# $\mathcal{H}_\infty$-based Control Design for Grid-forming Inverters with Enhanced Damping and Virtual Inertia

Dayan B. Rathnayake, *Student Member, IEEE,* Si Phu Me, *Student Member, IEEE,*
Reza Razzaghi, *Member, IEEE,* and Behrooz Bahrani, *Senior Member, IEEE*

***Abstract*—Grid-forming inverters (GFMIs) are identified as an important asset for achieving renewable energy-rich power grids. GFMIs are attracting significant attention due to their superior characteristics over grid-following inverters in both grid-connected (GC) and standalone (SA) scenarios. In this paper, a second-order discrete-time controller is proposed to achieve a well-damped step response for power reference commands and improved virtual inertia provision capability. In this paper, a control design method based on $\mathcal{H}_\infty$ is proposed, which is based on the frequency response of the system, to tune the proposed controller. The proposed control design presents a methodical process to specify the desired performance indices through frequency-domain constraints. The performance of the controller is thoroughly validated analytically and through simulation results. The superior performance of the proposed controller over the virtual synchronous generator controller in terms of tracking performance and virtual inertia provision capability is verified through experimental results.**

***Index Terms*—droop control, grid-interfaced inverter, grid-forming inverter, inverter-based resource, virtual synchronous generator (VSG).**

THE transition to net zero emissions is driving the rapid integration of inverter-based resources (IBRs) into power systems. IBRs are classified primarily into two categories: 1) grid-forming inverters (GFMIs) and 2) grid-following inverters (GFLIs). GFMIs have attracted significant attention in recent years, as they can operate stably in weak grids and in the standalone (SA) mode [1], [2]. The step response for power reference changes must be well-damped in GFMIs to accurately follow the automatic generation controller (AGC) dispatch commands in the grid-connected (GC) mode. On the other hand, the provision of virtual inertia from GFMIs is vital to decelerate the rate of change of frequency (RoCoF) following a load change in low-inertia scenarios, e.g. SA mode. Therefore, in this paper, a novel controller for the active power controller (APC) in GFMIs is proposed to achieve a well-damped step response and a desired level of virtual inertia provision in GC and SA modes, respectively [3].

Grid-forming capabilities for inverters are first introduced for uninterruptible power supply systems [4]. The droop control structure used in such applications is derived from the synchronous machine governor action that facilitates parallel operation. Grid-supporting droop-controlled GFMIs in the GC mode are tuned to regulate the active and reactive powers to keep the angular frequency ($\omega$) and the voltage ($V$) within the statutory limits, respectively. In high-voltage transmission networks, where lines are predominately inductive, active power ($P$) and reactive power ($Q$) are independently controlled using $P-\omega$ and $Q-V$ droop controllers, respectively [4], [5]. $P-V$ and $Q-\omega$ droop controllers could be used in networks where the line is predominantly resistive [6]. Alternately, in some studies, a virtual impedance loop is designed to shape the impedance seen from the converter to eliminate the impact of the line resistance-to-reactance ratio on the primary controller [7]. In [8], an $\mathcal{H}_\infty$-based control design method for GFLIs and droop-controlled GFMIs is proposed. However, one of the significant shortcomings of the droop controller is the limited virtual inertia provisioning capability.

To avoid issues in low-inertia grids, control strategies that mimic the behavior of synchronous machines are proposed to introduce inertial and damping capabilities. To this end, the virtual synchronous machine (VISMA) concept is proposed in [9]. It is followed by several different control methods that incorporate inertial and damping properties into the primary control loop while operating the converter as a voltage source. To this end, the concepts of virtual synchronous generator (VSG) [10], power-synchronization controller [11], synchronous power controller [12], and Synchronverter [13] are introduced where the inertial property of the synchronous machine is emulated by replicating the likes of the swing equation.

Several other control techniques are developed based on the VSG principle to improve the transient behavior of GFMIs. The inertial response of GFMIs is enhanced by a fuzzy-based VSG controller proposed in [14]. An APC that simultaneously uses frequency and phase angle for active power control is proposed in [15] to decouple power reference tracking from virtual inertia design. An artificial intelligence-based method is proposed in [16] to damp the subsynchronous electromechanical inter-area power oscillations in the system. The active power and reactive power controller (RPC) of a VSG are tuned for inductive and resistive weak grids in [17]. A damping controller is added to the VSG RPC in [18] to improve the damping. Robust controllers are designed based on an analytical method in [19] for the active power loop and the DC link control loop of a power-synchronization controller.

The GFMIs in the GC mode aim to precisely track the AGC dispatch commands. At the same time, the provision of virtual inertia from GFMIs to slow the RoCoF after a disturbance is critical in the SA mode. However, since the damping ratio and bandwidth of the closed-loop system with a VSG controller are intrinsically related to the droop coefficient and the inertia constant, the VSG controller cannot meet both objectives simultaneously [12], [20]. Therefore, a VSG controller with

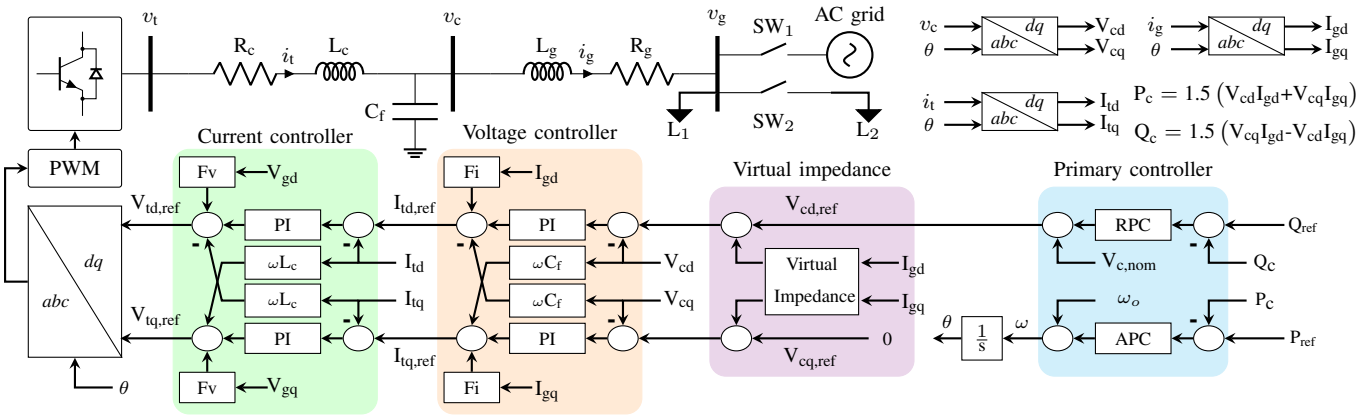


Fig. 1. A GFMI with internal controllers.

a low overshoot and short settling time for a step input in the GC mode could cause a large RoCoF in the SA mode. On the other hand, a VSG controller capable of providing high virtual inertia in the SA mode could result in a large overshoot and a long settling time for a step input in the GC mode.

Incorporating more poles and zeros into the APC design could fulfill the control objectives in the GC and SA modes. To this end, in [12], a lead controller is proposed. The additional zero in the lead controller defines the damping coefficient and bandwidth of the closed-loop system without affecting the intrinsic P-$\omega$ droop. However, the initial RoCoF after a load change in the SA mode is not considered in the control design. Therefore, the initial RoCoF following a load disturbance in the SA mode is very high due to the structure of the proposed controller. An $\mathcal{H}_\infty$-based high-order controller is proposed in [21] to damp the synchronous oscillations in a low-medium-voltage network. The operation of the GFMI in the SA mode is not taken into account in this work. Therefore, RoCoF constraint compliance is not considered in the design process. The generalized droop controller (GDC), which is a second-order controller, is proposed in [20] to fulfill the control objectives in the GC and SA modes. The control design of the GDC is based on trial and error, and directly defining the time-domain indices such as overshoot and rise time in the GC mode and initial RoCoF in the SA mode subsequent to a load disturbance is impossible. The generalized virtual synchronous generator (GVSG) control is proposed in [22] to achieve control objectives in both GC and SA modes. Direct equations are derived on the basis of the open-loop system to calculate the controller gains. However, calculating control gains using the given equations could lead to suboptimal controllers in bulk power systems, as the plant model is assumed to be a simple gain.

A second-order discrete-time controller and an $\mathcal{H}_\infty$-based control design method are proposed in this paper to design a APC that satisfies the control requirements in both GC and SA modes. The proposed control design method tunes the proposed controller to achieve a well-damped step response for power reference changes in the GC mode without causing large overshoots and oscillations in the SA mode. Furthermore, the proposed controller enhances the virtual inertia provision capability and conforms to the RoCoF relay withstand limits subsequent to a step load change in the SA mode.

The contributions of this paper are threefold:

1) a novel second-order discrete-time controller is proposed to achieve a well-damped step response for power reference changes in the GC mode while adhering to the RoCoF relay withstand limit in the SA mode.
2) a methodical formulation of the performance specifications such as overshoot, rise-time, $P-\omega$ droop coefficient, and RoCoF relay withstand limit compliance in the SA mode as frequency-domain constraints on the $\infty$-norm of sensitivity functions is presented.
3) the design of the proposed controller supports both parametric models or experimentally identified non-parametric frequency domain models of the plant as the constraints are formulated in the frequency domain.

The structure of the remainder of the paper is as follows. Section I discusses the performance of the VSG controller in the GC and SA modes. Then, the proposed control design process is presented in Section II. The simulation and experimental results are presented in Section III. Finally, conclusions are drawn in Section IV.

## I. Damping and Virtual Inertia Provision with the VSG Controller

### A. Test System Considered

Fig. 1 shows the complete control block diagram of the test system considered in this paper. In this paper, a typical GFMI with inner control loops is considered. In contrast to GFMIs without inner loops, cascaded control loops in GFMIs enable current limiting capabilities during faults [23], [24]. Therefore, in this paper, a GFMI with inner control loops is considered. Nonetheless, the controller proposed in this paper is applicable to GFMIs without inner control loops. As shown in Fig. 1, the inner control loops of GFMI consist of an inner current control loop, an intermediate voltage control loop, and a virtual impedance loop. The primary controller comprises an APC and an RPC. Note that the proposed control approach is similarly applicable to the RPC loop to control the voltage amplitude. However, in this paper, droop control is used for the RPC. When the grid impedance is predominately inductive, the voltage angle ($\theta$) and the magnitude ($V_{cd,ref}$) of the voltage

at the point of common coupling (PCC) ($v_c$) are independently controlled by the APC and RPC, respectively. This paper focuses on the APC of the primary controller. Two modes of operations of the GFMI are considered in this paper. First, the switch $\mathrm{SW}_1$ is kept closed, while the switch $\mathrm{SW}_2$ is kept open to operate the GFMI in the GC mode. Second, both $\mathrm{SW}_1$ and $\mathrm{SW}_2$ are kept open to operate the GFMI in the SA mode.

The power injected into the system shown in Fig. 1 is expressed as [25], [26],

$$P = \frac{3}{\mathrm{R_g^2 + X_g^2}}(\mathrm{R_g V_c^2 - R_g V_c V_g}\cos(\theta) + \mathrm{X_g V_c V_g}\sin(\theta)), \tag{1}$$

where $\mathrm{V_g}$ and $\mathrm{V_c}$ are the RMS quantities of the grid and capacitor voltages, respectively, and $\theta$ is the difference between the power angles. Moreover, $\mathrm{R_g}$ is the resistance and $\mathrm{X_g} = \omega \mathrm{L_g}$ the reactance of the line impedance. Hence, the small-signal model for active power deviations over angle deviations ($\Delta P/\Delta\theta$) is obtained as

$$\frac{\Delta P}{\Delta \theta} = 3\,\frac{\mathrm{X_g V_c V_g}\cos(\theta) + \mathrm{R_g V_c V_g}\sin(\theta)}{\mathrm{R_g^2 + X_g^2}} \tag{2}$$

where $\Delta$ is the increment operator.

The $\mathrm{X_g}$ is significantly larger than $\mathrm{R_g}$ if the line impedance is reactive in nature (e.g. in transmission networks). Hence, $\mathrm{R_g}$ is negligible. Furthermore, the trigonometric relationships given by $\sin(\theta) \rightarrow \theta$ and $\cos(\theta) \rightarrow 1$ are also valid as the power angle $\theta$ is generally small [26]. Finally, $\Delta\theta$ is substituted with $\Delta\omega/s$ to derive the parametric small-signal model for active power flow into the power grid over frequency ($G(s)$) as

$$G(s) = \frac{\Delta P}{\Delta \omega} = 3\,\frac{\mathrm{V_g V_c}}{\omega \mathrm{L_g}}\frac{1}{s} = \frac{\mathrm{k_g}}{s}, \tag{3}$$

where $\mathrm{k_g}$ is the plant gain and is equal to $3\mathrm{V_g V_c}/\omega \mathrm{L_g}$.

### *B. Parameter Tuning in the VSG Controller*

The control structure of the VSG controller is shown in Fig. 2. The control law for the VSG controller is defined as

$$K_{\mathrm{VSG}}(s) = \frac{\mathrm{D_p}}{(J\omega_0 \mathrm{D_p} s + 1)} = \frac{\mathrm{D_p}}{(\tau_i s + 1)}, \tag{4}$$

where $\mathrm{D_p}$, $J$, and $\tau_i = J\omega_0 \mathrm{D_p}$ are the steady-state droop coefficient, rotational inertia, and inertial time constant, respectively. The grid operator mandates the IBRs to support the grid during power system events. $\mathrm{D_p}$ is chosen such that in the steady-state, a full active power output, which is equal to the rating of the inverter ($\mathrm{S_n}$), is observed in the output power of the inverter for a predetermined frequency change ($\Delta\Omega$). Hence, $\mathrm{D_p}$ is obtained as

$$\mathrm{D_p} = \frac{\Delta \Omega}{\mathrm{S_n}}. \tag{5}$$

For IBRs, $\mathrm{D_p}$ may be lower than the droop coefficient of traditional synchronous generators, which is typically around 4% [12]. For example, a droop coefficient of roughly around 1.72% is set in the Hornsdale battery in South Australia [27].

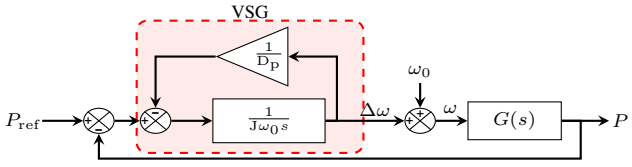


Fig. 2. Control block diagram of the VSG controller.

One of the pivotal characteristics of the VSG controller is that the VSG controller can provide virtual inertia. Therefore, $\tau_i$ is chosen based on the virtual inertia provision. Virtual inertia slows down RoCoF following a contingency. Therefore, the virtual inertia provisioning capability is quantified based on the RoCoF following a load disturbance. The frequency dynamics following a load disturbance can be modeled as

$$\frac{\Delta \omega}{\Delta P_{\mathrm{load}}} = \frac{-\mathrm{D_p}}{(\tau_i s + 1)}. \tag{6}$$

Consequently, $\Delta\dot{\omega} = s\Delta\omega$ and $\Delta P_{\mathrm{load}} = \mathrm{S_n}/s$ are substituted in (6) and the initial value theorem is applied to calculate the initial RoCoF ($\Delta\dot{\omega}|_{t\,=\,0^+}$) following a step load change of size $\mathrm{S_n}$ as

$$\begin{aligned}\Delta\dot{\omega}|_{t\,=\,0^+} &= \lim_{s\rightarrow\infty} s\,\frac{s\,(-\Delta\Omega/\mathrm{S_n})}{(\tau_i s + 1)}\,\frac{\mathrm{S_n}}{s} \\ &= \frac{-\Delta\Omega}{\tau_i}.\end{aligned} \tag{7}$$

Hence, $\tau_i$ is set such that the RoCoF resulting after a load disturbance is less than the RoCoF withstand capability of the RoCoF relays. Otherwise, the RoCoF relays could be activated and cause cascade tripping of other generators or damage equipment that is sensitive to RoCoF. As shown in (7), $\Delta\dot{\omega}|_{t\,=\,0^+}$ is less than a RoCoF level of $\rho$ up to a disturbance size of $\mathrm{S_n}$ only if $\tau_i \geq \Delta\Omega/\rho$ is satisfied. The number of different RoCoF relay settings, which could vary from 0.5 Hz/s to 2.5 Hz/s, are used in 50 Hz power systems. The standard RoCoF relay limits used in some power systems are as follows: Great Britain 0.5 Hz/s, Belgium 1 Hz/s, Ireland 1 Hz/s, South Africa 1 Hz/s, Denmark 2.5 Hz/s, and Spain 2 Hz/s [28].

### *C. Step Response of the GFMI with the VSG Controller*

The step response of the GFMI for a power reference change with the VSG controller can be evaluated on the basis of the closed-loop transfer function of the system. The analysis is carried out in the continuous-time domain as the concepts such as damping coefficient and bandwidth of a second-order system are commonly defined for continuous-time systems and widely used due to the relative ease of comprehension. Therefore, the closed-loop transfer function of the system with the VSG controller is derived using (3) and (4), and defined as

$$G_{\mathrm{cl}}^{\mathrm{VSG}} = \frac{\Delta P}{\Delta P_{\mathrm{ref}}} = \frac{\mathrm{D_p k_g}/\tau_i}{s^2 + s/\tau_i + \mathrm{D_p k_g}/\tau_i}. \tag{8}$$

As shown in (8), both the damping ratio ($\zeta = \sqrt{1/4\mathrm{D_p k_g}\tau_i}$) and natural frequency ($\omega_n = \sqrt{\mathrm{D_p k_g}/\tau_i}$), which directly affect the overshoot and settling time, respectively, depend directly on $\mathrm{D_p}$, $\tau_i$, and $\mathrm{k_g}$. Furthermore, according to (6) and (7),

TABLE I
PARAMETERS USED FOR SIMULATION TESTS AND EXPERIMENTS.

| Component | Description | Value |
|---|---|---|
| Grid | Strong grid (SCR = 10.6) | $L_g$ = 5.18 mH, $R_g$ = 0.15 Ω |
| | Weak grid (SCR = 1.9) | $L_g$ = 28.75 mH, $R_g$ = 0.5 Ω |
| | Grid voltage | $v_{g,L\text{-}L}$ = 130 $V_{RMS}$ |
| | Nominal frequency | $\omega_o$ = 314.15 rad $s^{-1}$ |
| GFMI | Filter parameters | $L_c$ = 7 mH, $R_c$ = 1 Ω, $C_f$ = 30 $\mu$F |
| | Capacitor voltage | $v_{c,L\text{-}L}$ = 130 $V_{RMS}$ |
| | Inverter rating | $S_{nom}$ = 1 kW |
| Droop | Damping gain | $D_p$ = $\pi$/1000 rad $s^{-1}$/W |
| | Inertial time constant | $\tau_i$ = 0.005 s |
| VSG | Damping gain | $D_p$ = $\pi$/1000 rad $s^{-1}$/W |
| | Inertial time constant | $\tau_i$ = 0.5 s |
| Loads | Standalone mode | $L_1$ = 500 W, $L_2$ = 850 W |

$D_p$ and $\tau_i$ directly affect the $\Delta\dot{\omega}|_{t\,=\,0^+}$ and the frequency trajectory following a step load disturbance.

The step response for a power reference change with the VSG controller for the test system illustrated in Fig. 1 is shown in Fig. 3(a). The parameters used in this analysis are given in Table I. $L_g$ and $R_g$ correspond to a grid with a short circuit ratio (SCR) of 3.9 are used. In addition, $D_p$ is set to 1% p.u., and $\tau_i$ is varied from 0.0455 s to 0.5 s.

As shown in Fig. 3(a), the overshoot and the settling time increase as $\tau_i$ increases. This is because, according to (8), both $\zeta$ and $\omega_n$ are decreased as $\tau_i$ is varied from 0.0455 s to 0.5 s. Therefore, both the overshoot and the settling time increase as the damping and bandwidth decrease, respectively. Additionally, the strength of the grid greatly influences the step response for a power reference change with the VSG controller. The value of $k_g$ increases as the strength of the grid increases. This causes $\zeta$ to decrease. Therefore, the damping of the system is greatly reduced as the system strength increases. This causes the step response for a power reference change in the GC mode with the VSG controller to have large overshoots.

On the other hand, as shown in Fig. 3(b), the frequency trajectory following a step load disturbance of size $S_n$ in the SA mode is improved as $\tau_i$ is increased from 0.0455 s to 0.5 s. The $\Delta\dot{\omega}|_{t\,=\,0^+}$ following the step load disturbance becomes much less as $\tau_i$ is increased from 0.0455 s to 0.5 s. This is because, according to (7), $\Delta\dot{\omega}|_{t\,=\,0^+}$ decreases as $\tau_i$ increases. Furthermore, the frequency variation over time is much slower as $\tau_i$ is increased. As shown in (6), the bandwidth decreases as $\tau_i$ increases. Hence, the initial RoCoF level is much smaller and the frequency variation over time is much slower as $\tau_i$ is increased. Therefore, according to the analysis, a high virtual inertia provision in the SA mode deteriorates the performance of the step response for a power reference change in the GC mode. On the other hand, a low overshoot and settling time in step response for power reference change in the GC mode result in a high RoCoF following a load disturbance in the SA mode.

The synchronous power controller (SPC) is proposed in [12] to separate the functions of droop and damping. SPC decouples the droop coefficient, damping, and inertia coefficient allowing to individually define the droop coefficient, damping ratio, and closed-loop bandwidth of the system without compromising the droop coefficient nor the inertial

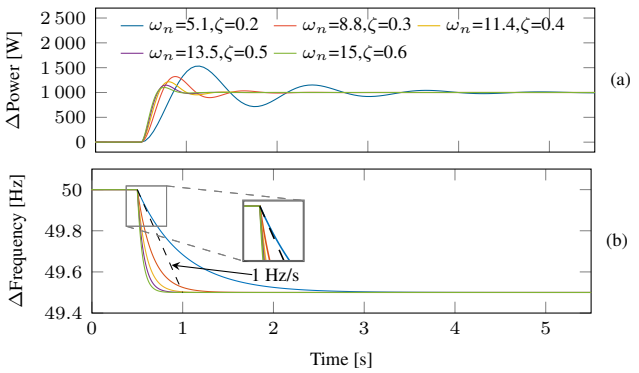


Fig. 3. Step response of (a) (8) in the GC mode and (b) (6) in the SA mode as $\tau_i$ is varied from 0.0455 s to 0.5 s.

time constant. The structure of the SPC is defined as

$$K_{\text{spc}}(s) = \frac{(k_p s + k_i)}{(s + k_j)}, \tag{9}$$

where $k_p$, $k_i$, and $k_j$ are set based on the required damping ratio, bandwidth, and $P-\omega$ droop characteristic, respectively. A critical shortcoming of the SPC is that it results in a very high initial RoCoF following a load disturbance in the SA mode. Similar to the analysis of the VSG, the frequency trajectory with the SPC after a load disturbance in the SA mode can be found by evaluating the response of

$$\frac{\Delta\omega}{\Delta P_{\text{load}}} = \frac{-(k_p s + k_i)}{(s + k_j)}. \tag{10}$$

The initial value theorem could be applied to (10) to derive an expression for the maximum upper bound for the $\Delta\dot{\omega}|_{t\,=\,0^+}$ with the SPC for a step load disturbance of the size equal to $S_n$ as follows:

$$\Delta\dot{\omega}|_{t\,=\,0^+} = \lim_{s\to\infty} s\ \frac{s\ (-(k_p s + k_i))}{(s + k_j)}\ \frac{S_n}{s} \to \infty. \tag{11}$$

As shown in (11), due to the biproper structure of the SPC $\Delta\dot{\omega}|_{t\,=\,0^+}$ with the SPC becomes extremely high.

As shown in Fig. 3, inherently, there is a trade-off between the step response for power reference changes in the GC mode and the initial RoCoF that results after a load disturbance in the VSG controller. As shown in Fig. 3, if a VSG controller is capable of providing high virtual inertia to conform to the RoCoF relay withstand limit in the SA mode, a large overshoot and a long settling time result in the step response of the power in the GC mode. On the other hand, if the VSG controller results in a low overshoot and short settling time in step response in the GC mode, the virtual inertia provision capability of the GFMI with VSG becomes limited. An $\mathcal{H}_\infty$-based approach is proposed in this paper to overcome the shortcomings of the VSG controller. A discrete time second-order controller and an $\mathcal{H}_\infty$-based control design is proposed in this paper to track the power reference commands with enhanced damping in the GC mode while enhancing the virtual inertia capability of the GFMI to conform to the RoCoF relay withstand limit in the SA mode.

## II. $\mathcal{H}_\infty$-BASED CONTROL DESIGN

The APC design based on the proposed $\mathcal{H}_\infty$ control design method is elaborated in this section. A frequency-domain control design method that guarantees robust stability and performance is proposed to tune the controller gains. The design guidelines for the proposed $\mathcal{H}_\infty$-based control design include the following steps:

1) obtain the frequency response of the plant.
2) define the structure and the order of the controller.
3) define the performance indices as frequency-domain constraints.
4) solve the convex optimization problem to obtain the discrete-time controller gains.

Each of the steps of the proposed control design is thoroughly elaborated in the following.

### A. Frequency Response Data Model Identification

The fixed-structure robust control design method presented in this paper is based on the frequency response ($G(j\omega) \in \mathbb{C}$) of the system to be controlled. $G(j\omega)$ is assumed to be bounded in all frequencies except a finite number of frequencies that correspond to the poles of $G(j\omega)$ on the imaginary axis. The $G(j\omega)$ can be obtained from either the parametric model of the system or experimentally.

The proposed control design is capable of working with an experimentally identified frequency response of the system. This is particularly advantageous when working with high-order plant models, where complex dynamics that are difficult to model are involved. Therefore, a typical system identification method can be used to identify the frequency response of the system. One such method is exciting the system using a pseudorandom binary sequence (PRBS). PRBS excitation for model identification is adopted in academic research and industry studies [29]–[32].

The closed-loop model of the system given in Fig. 1 and Table I is experimentally identified in this paper with a laboratory setup using the PRBS signal injection. To this end, the power reference ($\mathrm{P_{ref}}$) of the GFMI is superimposed with a maximum length PRBS signal. Any stable controller can be used for closed-loop identification. Therefore, in this paper, a droop controller defined as $K_{\mathrm{Droop}}(s) = \mathrm{D_p}/(0.005s+1)$ is used during the closed-loop identification. Typically, the cutoff frequency of the lowpass filter in $K_{\mathrm{Droop}}(s)$ is chosen high enough to filter out high-frequency harmonics [33]. Since the bandwidth of $K_{\mathrm{Droop}}(s)$, which is 200 rad s$^{-1}$, is much higher than the frequency range of interest, the frequency spectrum of the PRBS signal is not distorted by $K_{\mathrm{Droop}}(s)$.

The power spectral density of the PRBS signal is similar to that of white noise. Therefore, the PRBS signal is considered as an approximation of discrete white noise. Linear feedback shift registers are used to generate the PRBS signal, which is a discrete signal that repeats itself. The data length ($l$) of a $b$-bit PRBS signal is

$$l = 2^{b-1}. \tag{12}$$

The sampling time ($\mathrm{T}_i$) and $b$ of the maximum length PRBS signal must be chosen such that $1/\mathrm{T}_i$ is large enough to capture the high-frequency features. Simultaneously, $1/(l\mathrm{T}_i)$ is small enough to capture the salient low-frequency content while attaining the preferred frequency resolution. The preferred frequency resolution of the identified frequency response can be increased by choosing a higher bit number for $b$. Furthermore, the identified frequency range can be increased by reducing $\mathrm{T}_i$. A 10-bit maximum length PRBS with a sampling time of 20 ms is used in this paper. The corresponding output power ($\mathrm{P_c}$) is measured once the system is excited with a PRBS signal superimposed on $\mathrm{P_{ref}}$. The PRBS signal and $\mathrm{P_c}$ are shown in Fig. 4. The parameters used for the system identification are given in Table II.

TABLE II
SYSTEM IDENTIFICATION PARAMETERS.

| Parameter | Description | Value |
|---|---|---|
| $\mathrm{T}_i$ | Identification sampling time | 20 ms |
| $b$ | Length of shift register | 10 |
| $\alpha$ | Amplitude of PRBS | 100 W |
| $l$ | Data length | 1023 |

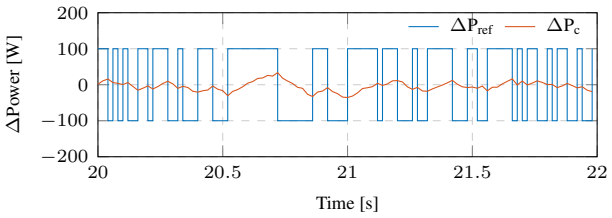


Fig. 4. The PRBS signal injected and the corresponding measured power.

Once the input data ($\mathrm{P_{ref}}$) and output ($\mathrm{P_c}$) data is collected, the frequency response data (FRD) of the closed-loop model of the system can be identified. In this paper, the system identification toolbox in Matlab is used for the FRD model identification of the closed-loop model of the system. Since the open-loop model of the system is required for the control design, it is obtained from the identified closed-loop model of the system as

$$G(e^{j\omega}) = \frac{G_{\mathrm{cl}}(e^{j\omega})}{(1 - G_{\mathrm{cl}}(e^{j\omega}))K_{\mathrm{Droop}}(e^{j\omega})}, \tag{13}$$

where $G(e^{j\omega})$, $G_{\mathrm{cl}}(e^{j\omega})$, and $K_{\mathrm{Droop}}(e^{j\omega})$ are the frequency response of the identified open-loop model, the frequency response of the identified closed-loop model, and the frequency response of $K_{\mathrm{Droop}}(z)$, respectively.

$G(e^{j\omega})$ and the frequency response of the parametric model derived from (3) are shown in Fig. 5. As shown in Fig. 5, the experimentally identified model accurately captures the dynamics of the open-loop model.

### B. The Proposed Controller Structure

The proposed controller is defined as

$$\Delta\omega(z) = K(z)\ \Delta\mathrm{P}(z) \tag{14}$$

in which $K(z) = X(z) \cdot Y(z)^{-1}$ where

$$X(z) = [x_2 z^2 + x_1 z^1 + x_0], \tag{15}$$
$$Y(z) = [z^2 + y_1 z^1 + y_0]. \tag{16}$$

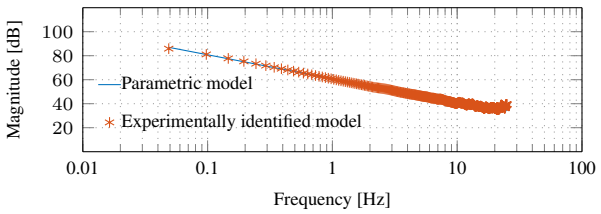


Fig. 5. The parametric and experimentally identified open-loop model of the system in the frequency-domain.

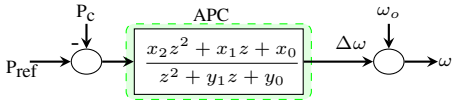


Fig. 6. Control block diagram of the proposed controller.

$X(z)$ and $Y(z)$ are polynomials in the $z$-domain. $[x_2, x_1, x_0]$ and $[y_1, y_0]$ specify the controller gains that need to be tuned. The control block diagram of the proposed controller is shown in Fig. 6. The controller is presented in the discrete-time domain in (14) as the implementation is done in a digital signal processor. However, note that for the control design, only the frequency response of the controller is used/needed. Therefore, if the designer prefers a continuous-time controller, that too can be designed since only the frequency response is used in the control design. However, continuous-time controllers must be discretized to be implemented in a microcontroller.

As shown in Section I, a first-order controller such as the VSG controller cannot attain good performance in both GC and SA modes. Therefore, more zeros and poles must be incorporated to appropriately shape the singular value responses of the sensitivity functions over a range of frequencies to achieve the required performance in the GC and SA modes. Typically, low-order controllers are preferred over high-order controllers as they are easier to implement and numerically stable. Therefore, in this paper, a second-order discrete-time controller as shown in Fig. 6 is proposed.

### C. Specifying Controller Performance as Constraints

*1) Achieving the Desired Tracking Performance and Disturbance Rejection in the GC Mode:* The required performance specifications of the controller in the GC and SA modes are defined as constraints on the norm of the sensitivity functions. Therefore, a mixed-sensitivity problem is considered in this paper. In the GC mode, the primary objective of the GFMI is to accurately follow the power reference signals. To this end, the $\infty$-norm of the output sensitivity function ($\mathcal{S}(e^{j\omega})$) is considered to achieve acceptable tracking performance and output disturbance rejection. $\mathcal{S}(e^{j\omega})$ is defined as

$$\mathcal{S}(e^{j\omega}) \;=\; \frac{1}{(1+G(e^{j\omega})K(e^{j\omega}))}. \tag{17}$$

Therefore, the sensitivity problem is defined as

$$\min_{K} \; \|W_1\mathcal{S}\|_\infty \,, \tag{18}$$

where $W_1$ is the performance weighting function on $\mathcal{S}(e^{j\omega})$. The specifications of the objective function can be roughly denoted as $|\mathcal{S}(e^{j\omega})| \;\leq\; 1/|W_1(e^{j\omega})|$ [34]. Generally, the low-frequency gain of $\mathcal{S}(e^{j\omega})$ is kept low since then only the closed-loop system will be able to properly track the reference for step input signals. Furthermore, the peak of $\mathcal{S}(e^{j\omega})$ directly corresponds to the damping of the closed-loop system, and the overshoots could be excessive if the peak of $\mathcal{S}(e^{j\omega})$ is too high. Therefore, the high-frequency gain of $\mathcal{S}(e^{j\omega})$ is constrained such that the overshoot in the output of the closed-loop system for step inputs is within acceptable limits [34]. A suitable performance weighting function on $\mathcal{S}(e^{j\omega})$ is

$$W_1(s) = \left(\frac{s/\sqrt[\lambda]{M_s} + \omega_b}{s + \omega_b \sqrt[\lambda]{\varepsilon_s}}\right)^{\lambda}, \tag{19}$$

where $M_s$, $\omega_b$, and $\varepsilon_s$ are the peak sensitivity, closed-loop bandwidth, and acceptable steady-state error for a step disturbance, respectively. $\lambda \in \mathbb{Z}^+$ can be increased for a steeper roll-off between low-frequency and high-frequency [34]. Therefore, the maximum overshoot for a step input in the GC mode can be minimized by specifying a low value for $M_s$. $W_1(s)$ is discretized using the bilinear transform, and its frequency response ($W_1(e^{j\omega})$) is used in the control design.

*2) Achieving the RoCoF Relay Compliance in the SA Mode:* In the SA mode, no inertia is available from the synchronous machines, as the GFMI is disconnected from the grid. Therefore, the main concern in the SA mode is the RoCoF relay withstanding limit following load power changes. Hence, in this paper, the control effort in the high-frequency is minimized to attenuate large frequency excursions following load disturbances in the SA mode. To this end, the high-frequency gain of $K(z)$ is minimized in this paper to guarantee the RoCoF relay withstand capability. This can be denoted as $|K(e^{j\omega})| \leq |K^{\rho}_{\text{vsg}}(e^{j\omega})|$, where $|K^{\rho}_{\text{vsg}}(e^{j\omega})|$ is the VSG controller that conforms to a RoCoF withstand level of $\rho$. Therefore, the following constraint is defined as

$$\|W_2K\|_\infty \;<\; 1, \tag{20}$$

where $W_2(e^{j\omega})$ is the weighting function of the controller, which is considered to limit the high-frequency gain of the controller.

These control specifications of the controller can be roughly denoted as $|K(e^{j\omega})| \;\leq\; 1/|W_2(e^{j\omega})|$ [34]. Hence, a candidate for $W_2(e^{j\omega})$ can be derived based on $|K^{\rho}_{\text{vsg}}(e^{j\omega})|$. As shown in Section I, the initial RoCoF in the SA mode with a VSG controller conforms to $\rho$ up to a disturbance size equal to $\mathrm{S_n}$ only if $\tau_i \geq \Delta\Omega/\rho$. Therefore, a candidate transfer function for $W_2(e^{j\omega})$ can be defined as

$$W_2(s) = \frac{\tau_i^{\rho} s + 1}{\mathrm{D_p}(\varepsilon_2 s + 1)}, \tag{21}$$

where $\tau_i^{\rho} = \Delta\Omega/\rho$ is the minimum $\tau_i$ that can withstand a RoCoF level of $\rho$ and $\varepsilon_2$, which is a small value, is added to make $W_2(s)$ proper. $W_2(s)$ is discretized using the bilinear transform, and its frequency response ($W_2(e^{j\omega})$) is used in the control design. In this paper, $\rho$ is considered to be 1 Hz / s.

*3) Specifying the $P-\omega$ Droop Coefficient:* Finally, the desired $P-\omega$ droop characteristic is set using the steady-state gain of the controller. The steady-state gain of the controller is expressed as a constraint in the frequency domain by

evaluating the gain of the controller at the first frequency point, which is $\omega$ = 0 rad/s. The gain of the controller at $\omega$ = 0 rad/s is evaluated as

$$\frac{x_2 + x_1 + x_0}{1 + y_1 + y_0} = \mathrm{D_p}, \tag{22}$$

where $[x_2,\ x_1, x_0]$ and $[y_1, y_0]$ are the coefficients of the numerator and denominator polynomials of the controller, respectively, and $\mathrm{D_p}$ is the desired $P-\omega$ droop coefficient. In this paper, $\mathrm{D_p}$ is chosen as $\pi/1000$ Hz/W.

*4) Stability of the Closed-loop System:* The closed-loop stability of the system with $G$ and $K$ as transfer functions of the plant and the controller, respectively, is guaranteed if and only if

1) the Nyquist plot of the open-loop transfer function does not pass through the critical point, which is -1+0$j$, and
2) the number of encirclements around the critical point is equal to the sum of the poles of $G$ and $K$ that are on the exterior of the unit circle.

The modulus margin ($M$), which makes the system robustly stable, is considered in (18) as $M$ is defined as

$$M \ = \ \left(\sup_{\omega} \bar{\sigma}[\mathcal{S}(e^{j\omega})]\right)^{-1} \tag{23}$$

where $\|\mathcal{S}\|_\infty \ = \ \sup_\omega \bar{\sigma}[\mathcal{S}(e^{j\omega})]$. $M$ guarantees the widely known gain and phase margin simultaneously since $M$ corresponds to the minimum distance from the Nyquist plot of the open-loop transfer function to the critical point. Therefore, the first condition for a stable closed-loop system is guaranteed. Hence, a distance is always guaranteed between the Nyquist plot of the open-loop transfer function and the critical point. However, $M$ does not guarantee the second condition for a stable closed-loop system. This is further discussed in Section II-D.

### *D. Convex Optimization Problem Formulation*

The optimization problem described in Section II-C is nonconvex. Therefore, in this section, the formulation of the convex optimization problem is discussed. Since the ensuing discussion is in the frequency domain, the term $(e^{j\omega})$ is omitted from the transfer functions for ease of notation.

The optimization problem defined in Section II-C is converted to a problem on the spectral norm as

$$\min_{X,Y} \quad \gamma \tag{24a}$$

$$\text{s.t.} \quad \left[W_1\mathcal{S}\right]^* \left[W_1\mathcal{S}\right] < \gamma I \quad \forall\omega \ \in \ \Omega, \tag{24b}$$

$$\left[W_2K\right]^* \left[W_2K\right] < I \quad \forall\omega \ \in \ \Omega, \tag{24c}$$

$$(x_2 + x_1 + x_0) \ - \ \mathrm{D_p}(1 + y_1 + y_0) \ = \ 0 \tag{24d}$$

where $\gamma$ is an upper bound on the $\infty$-norm of $W_1\mathcal{S}$, and $\{\}^*$ denotes the conjugate transpose operation. The objective function is represented as minimizing $\gamma$ under the constraints (24b), (24c), and (24d). Therefore, the objective function and the constraints defined in (18), (20), and (22) in the original optimization problem in Section II-C are equivalent to (24b), (24c), and (24d), respectively.

The constraint in (24b) is converted to convex form in the following as an example to describe the general convexification procedure used in this paper. The first step to convexify the constraint in (24b) is to rewrite it as

$$\left[W_1Y(Y+GX)^{-1}\right]^* \left[W_1Y(Y+GX)^{-1}\right] \ < \ \gamma I \quad \forall\omega \ \in \ \Omega \tag{25}$$

and then converted to convex-concave form as

$$Y^*W_1^*\gamma^{-1}W_1Y - (Y+GX)^*(Y+GX) \ < \ 0 \quad \forall\omega \ \in \ \Omega. \tag{26}$$

Let $J \ = \ (Y + GX)$ and $J_c \ = \ (Y_c + GX_c)$ where $X_c$ and $Y_c$ are the denominator and numerator, respectively, of a known stabilizing initial controller defined as $K_\mathrm{c} \ = \ X_cY_c^{-1}$. Consequently, the concave part $JJ^*$ is linearized around $J_c$ using the Taylor expansion as $JJ^* \ \approx \ J^*J_c + J_c^*J - J_c^*J_c$. As a result, an inner convex approximation of the original optimization problem is reached. Therefore, a sufficient convex constraint for (26) is obtained as

$$Y^*W_1^*\gamma^{-1}W_1Y - J^*J_c - J_c^*J + J_c^*J_c \ < \ 0 \quad \forall\omega \ \in \ \Omega. \tag{27}$$

Finally, the Schur complement is used to represent (27) as a linear matrix inequality (LMI) as follows

$$\begin{bmatrix} \gamma I & W_1Y \\ (W_1Y)^* & J^*J_c + J_c^*J - J_c^*J_c \end{bmatrix} \ > \ 0. \tag{28}$$

Similarly, (24c) is converted to a convex constraint to obtain the full convex optimization problem. A complete theoretical exposition is given in [35]. The entire convex optimization problem is summarized as

$$\min_{X,Y} \quad \gamma \tag{29a}$$

$$\text{s.t.} \quad \begin{bmatrix} \gamma I & W_1Y \\ (W_1Y)^* & J^*J_c + J_c^*J - J_c^*J_c \end{bmatrix} > 0 \qquad \forall\omega\in\Omega, \tag{29b}$$

$$\begin{bmatrix} I & W_2X \\ (W_2X)^* & Y^*Y_c + Y_c^*Y - Y_c^*Y_c \end{bmatrix} > 0 \qquad \forall\omega\in\Omega, \tag{29c}$$

$$(x_2 + x_1 + x_0) \ - \ \mathrm{D_p}(1 + y_1 + y_0) = 0 \tag{29d}$$

The objective function is represented as minimizing $\gamma$ under constraints (29b) and (29c), which includes minimizing the output sensitivity and the high-frequency gain of the controller. The equality (29d) indicates the constraint on the $P-\omega$ droop coefficient.

The second condition to guarantee the stability of the closed-loop system discussed in Section II-C4 is ensured by satisfying the following conditions, as explained below. A complete theoretical exposition of the stability analysis based on the generalized Nyquist theorem is given in [35]. However, the salient conditions that ensure the closed-loop stability of the system are summarized below. The stability of the closed-loop system is guaranteed if

- $\det(Y) \neq 0$. This is ensured by guaranteeing $YY^* > 0$. This inequality is linearized and used in the optimization problem in the constraint (29c) as $Y^*Y_c + Y_c^*Y - Y_c^*Y_c$.
- the final controller and the initial controller must share the same poles on the unit circle. In this paper, there are no poles on the unit circle in the initial controller or the final controller.
- the order of $\det(Y_c)$ must be equal to $\det(Y)$. This condition is satisfied by adding the desired number of poles and zeros at the origin to augment the initial controller without affecting it.

In theory, the control design method is defined for an infinite number of frequency points. Therefore, it contains an infinite number of constraints. Typically, an infinite number of frequency points is replaced by a finite set of frequencies such as $\Gamma = \{\omega_N = \frac{N\pi}{dT_s} | N = 0, \cdots, d\}$, where $d$ and $T_s$ are the number of frequency points considered and the sampling time of the controller, respectively, to overcome this issue. A reasonably large set of frequencies is chosen without affecting the solver time, as the complexity of the problem increases linearly with the number of constraints.

One implication of the inner approximation made of the original optimization problem is that the resulting controller could be a suboptimal controller that is far from the control specifications defined in the original optimization problem. Therefore, the optimization problem is solved iteratively, where the resulting suboptimal controller is used as $K_\mathrm{c}$ in the subsequent iteration. Thus, the solution finally converges to a local optimum of the original problem.

### *E. Obtaining Controller Gains for the Test System Considered*

The proposed controller is designed based on the proposed control design for the GFMI given in Fig. 1 and Table I. The strong grid condition is used to design the controller, although the performance of the controller is validated later for a weak grid condition as well. The parameters used in the control design are listed in Table III. A VSG controller defined as $K_\mathrm{VSG}(s) = (\pi/1000)/(2s+1)$ is used as $K_\mathrm{c}$. In this study, a droop gain of $\pi$/1000 rad s$^{-1}$/W and a RoCoF constraint of 1 Hz/s are considered. The optimization problem is formulated using YALMIP [36] and solved by MOSEK [37]. The algorithm converges in 17 iterations and takes about 20 minutes on a standard desktop computer.

The singular value response (SVR) of $\mathcal{S}$ with the initial controller ($\mathcal{S}_{K_\mathrm{c}}$), the proposed controller ($\mathcal{S}_{K_{\mathcal{H}\infty}}$), and the SVR of the inverse of the performance weighting filter ($1/W_1$) are shown in Fig. 7(a). Fig. 7(a) clearly shows the reduction of the maximum singular value (MSV) of $\mathcal{S}_{K_{\mathcal{H}\infty}}$ over the frequency range considered. For example, the MSV of $\mathcal{S}_{K_\mathrm{c}}$ is 14.1 dB, and it is reduced to a value of 2.64 dB in the MSV of $\mathcal{S}_{K_{\mathcal{H}\infty}}$. The MSV of $\mathcal{S}$ is directly related to the damping. Therefore, the damping increases and the oscillations and overshoots are attenuated when the MSV of $\mathcal{S}_{K_{\mathcal{H}\infty}}$ is reduced.

The SVR of $K_\mathrm{c}$, $K_{\mathcal{H}\infty}$, and the inverse of the input weighting filter ($1/W_2$) are shown in Fig. 7(b). The most important factor in $\|K_{\mathcal{H}\infty}\|_\infty$ is the high-frequency gain, as it is directly related to the initial RoCoF in the SA mode. Thus, RoCoF compliance is guaranteed by limiting the high-frequency gain of $\|K_{\mathcal{H}\infty}\|_\infty$. As seen in Fig. 7(b), the high-frequency gain of $K_{\mathcal{H}\infty}$ is kept below $1/W_2$ to ensure RoCoF compliance. The final controller is

$$K_{\mathcal{H}\infty}(z) = \frac{10^{-5}(5.7495z^2 + 0.2376z - 5.5108)}{z^2 - 1.7914z + 0.7929} \tag{30}$$

TABLE III
DATA USED FOR CONTROL DESIGN.

| Parameter | Value | Description |
|---|---|---|
| $W_1$ | Performance weighting function | $\omega_b$ = 1, $M_s$ = 1.6, $\varepsilon_s$ = 0.0001, $\lambda$ = 2 |
| $W_2$ | Controller weighting function | $\varepsilon_2 = 10^{-6}$, $\tau_i^\rho$ = 0.5 s, $\mathrm{D_p}$ = $\pi$/1000 rad s$^{-1}$/W |
| $\mathrm{D_p}$ | $P-\omega$ droop coefficient | $\pi$/1000 rad s$^{-1}$/W |
| $\rho$ | RoCoF relay withstand limit | 1 Hz/s |
| $T_s$ | Sampling time | 20 ms |
| $d$ | Number of frequency points | 1023 |

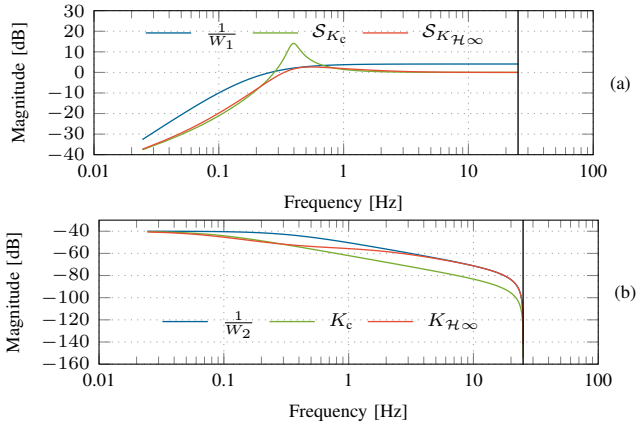


Fig. 7. Singular value plots of (a) $1/W_1$, $\mathcal{S}_{K_\mathrm{c}}$, $\mathcal{S}_{K_{\mathcal{H}\infty}}$ and (b) $1/W_2$, $\mathcal{K}_\mathrm{c}$, $K_{\mathcal{H}\infty}$.

### *F. Performance Verification*

The performance of the proposed controller is tested in a simulation environment in Matlab/PLECS. The parameters and their values used in the simulation are listed in Table I. Furthermore, the performance of the proposed controller is tested against the performance of the droop and VSG controllers given in Table I. Note that the same values for $P-\omega$ droop coefficient and the RoCoF relay withstand limit considered during the control design of the proposed controller are used to design the droop and VSG controllers for a fair comparison. Therefore, the droop and VSG controllers employ a $P-\omega$ droop coefficient of 1 %, and the VSG controller is designed to conform to a RoCoF relay withstand limit of 1 Hz/s.

*1) Enhanced Damping in the Grid-connected Mode:* The primary objective of the GFMI in the GC mode is to achieve a well-damped step response for power reference step changes. The grid conditions are subject to changes during the operation

of the GFMI. Therefore, in this paper, the performance of the controller is tested against two different grid strengths. The strength of the grid is characterized on the basis of the SCR of the PCC. The SCR is defined as

$$\mathrm{SCR} = \frac{1}{\mathrm{Z_g^{p.u.}}}, \tag{31}$$

where $\mathrm{Z_g^{p.u.}}$ is the per unit (p.u.) grid impedance on $\mathrm{S_n}$ base. In this paper, SCRs of 10.6 and 1.9, which correspond to strong and weak grids, respectively, are used to validate the performance of the proposed controller.

In this test, the GFMI shown in Fig. 1 is operated in the GC mode, where $\mathrm{SW_1}$ and $\mathrm{SW_2}$ are kept closed and opened, respectively. A power reference change of 1 kW is applied to the grid-forming converter at t = 2 s. The simulation results for a power reference change of 1 kW in the GC mode in a strong grid and weak grid are shown in Fig. 8(a) and 8(b), respectively.

Step responses for an active change of power reference with the VSG control and the proposed controller in a strong grid (SCR = 10.6) are shown in Fig. 8(a). As shown in Fig. 8(a), the active power output with the VSG controller has a large overshoot of around 68% and a long settling time of about 4.7 s. On the other hand, the proposed controller has a low overshoot of approximately 26% and a settling time of about 2.1 s. Therefore, the proposed controller significantly outperforms the VSG controller in the GC mode on a strong grid. As shown in Fig. 8(a), the change in power output with a droop controller is the most well-tracked out of the three traces shown. Active power output with the droop controller has no overshoot and the settling time, which is 2.101 s, is significantly less than the other two controllers.

Step responses for an active change in power reference with the VSG controller and the proposed controller in a weak grid (SCR = 1.9) are shown in Fig. 8(b). As shown in Fig. 8(b), the active power output with the VSG controller has an overshoot of around 39% and a settling time of about 6.1 s. On the other hand, the proposed controller has an overshoot of approximately 32% and a settling time of about 5.85 s. Therefore, the proposed controller shows better performance than the VSG controller in the GC mode in a weak grid. As shown in Fig. 8(b), similar to the strong grid scenario, the change in power output with a droop controller is the most well-tracked out of the three traces shown. Active power output with the droop controller does not have an overshoot, and the settling time, which is 2.86 s, is significantly less than the other two controllers.

*2) Enhanced Virtual Inertia Provision in the Standalone Mode:* In this test, the virtual inertia provision capability of the controller is tested in a low-inertia scenario. To this end, $\mathrm{SW_1}$ is kept open to disconnect the GFMI from the grid and operate in the SA mode. The conformity to RoCoF relay withstand limit is used as the criteria to assess the virtual inertia provision capability of the proposed controller. In this test case, $\mathrm{SW_2}$ is closed at t = 2 s to connect load $\mathrm{L_2}$ to administer a load disturbance of 850 W.

The frequency variations over time with the droop, VSG, and the proposed controller for a load disturbance in the SA mode are shown in Fig. 9. The control parameters of the VSG controller are set such that the initial RoCoF with the VSG controller complies with the RoCoF relay withstand limit. Thus, the frequency trajectory with VSG controller can be considered as a guide to assess whether the RoCoF with the proposed controller is within the considered RoCoF relay withstand limit.

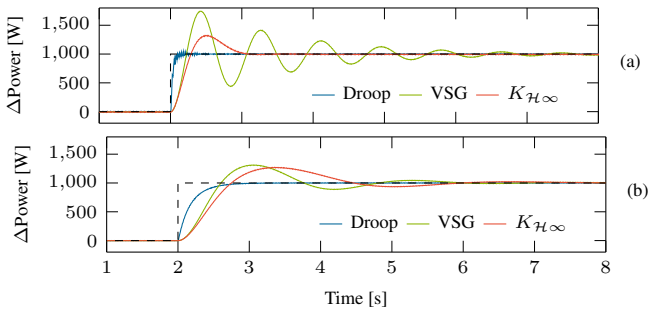


Fig. 8. Step response for a power reference step change of 1 kW in the GC mode with the VSG and proposed controllers in a (a) strong grid and (b) weak grid.

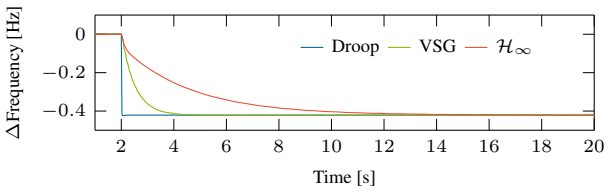


Fig. 9. Frequency change for a load change of 850 W in the SA mode with the VSG and proposed controllers.

As shown in Fig. 9, the frequency variation following a load disturbance with the droop controller is extremely fast due to the high bandwidth of the droop controller. Therefore, an extremely high initial RoCoF, which violates the RoCoF constraint considered in this study, is observed. High RoCoF levels are detrimental to some equipment and could trigger the tripping of sources that are highly sensitive to high RoCoF levels. As seen in Fig. 9, the initial RoCoF levels for the VSG controller and the proposed controller are similar. Hence, the initial RoCoF after a load disturbance with the proposed controller is the same, if not less, compared to the VSG controller. Therefore, the proposed controller adheres to the RoCoF relay withstand limit. Furthermore, the frequency variation after some time is much slower with the proposed controller than with the VSG controller, meaning that the proposed controller provides more inertia to the system than the VSG. Therefore, the proposed controller outperforms the VSG controller in the SA mode in terms of the initial RoCoF following a load disturbance and the enhanced virtual inertia provision capability.

## III. Experimental Validation

The proposed controller is tested in an experimental setup shown in Fig. 10 to further verify and corroborate the theoretical analysis and simulation results. The components of the experimental setup include a GFMI, line inductor, local load,

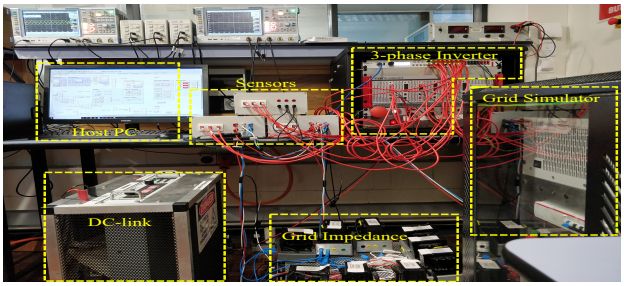


Fig. 10. Experimental setup.

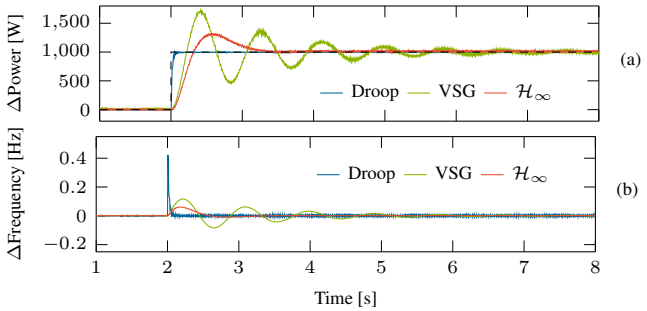


Fig. 11. Experimental results for a 1 kW step change in active power reference in the GC mode for a grid with SCR = 10.6: (a) step response of active power and (b) change in frequency.

remote load, and a grid simulator. The values used for the line inductor, local load, and remote load are the same as the values used in the simulation tests and are given in Table I. A 30 kVA Regatron TC.ACS three-phase grid simulator is used as the grid in the experimental setup. The internal structure of the GFMI is shown in Fig. 1, which includes a three-phase two-level inverter, internal control loops, an LC filter, and a dc source. An Imperix SiC-based power inverter is configured as a three-phase two-level inverter. Inner control loops are implemented in an Imperix BBox controller, which provides gate signals for the IGBTs. A MAGNA-POWER dc power supply set to 320 V is used as the dc source to feed the GFMI.

The performance of the proposed controller is compared against the performance of the droop and VSG controllers. Note that the same values for $P-\omega$ droop coefficient and the RoCoF relay withstand limit considered during the control design of the proposed controller are used to design the droop and VSG controllers for a fair comparison. Therefore, the droop and VSG controllers employ a $P-\omega$ droop coefficient of 1 %, and the VSG controller is designed to conform to a RoCoF relay withstand limit of 1 Hz/s.

Four types of scenarios are conducted to evaluate the performance of the proposed controller: 1) accurate power reference tracking in the GC mode, 2) RoCoF withstand capability in the SA mode, 3) frequency support capability during grid frequency variations, and 4) multi-inverter test. The test setup for the first three scenarios is shown in Fig. 1. In the GC mode, $SW_1$ is kept closed, while $SW_2$ is kept open. In the SA mode, initially, both $SW_1$ and $SW_2$ are kept open. At t = 2 s, $SW_2$ is closed, and $L_2$ is connected. Finally, in the frequency support capability test, $SW_1$ is kept closed while $SW_2$ is kept open. Then, the grid frequency is stepped down to 49.85 Hz to verify the response of the GFMI.

### *A. Enhanced Damping for Accurate Power Reference Tracking in the Grid-connected Mode*

The enhanced damping for the accurate power reference tracking performance in the GC mode of the proposed controller is experimentally validated to further verify the simulation results. Therefore, a reference tracking test in the GC mode is conducted using the experimental setup. To this end, the active power reference is changed by 1 kW to test the step response of the proposed controller and to compare the performance of the proposed controller with that of the droop and VSG controllers. Furthermore, the performance of the proposed controller is tested for two different grid strengths of SCR = 10.6 and SCR = 2.

*1) Strong Grid Scenario (SCR = 10.6):* The experimental results for the change in active power reference in the GC mode in a strong grid are shown in Fig. 11. Similarly to the simulation results, as shown in Fig. 11(a), the experimental results validate the superior performance of the proposed controller over the VSG controller in the GC mode. The proposed controller results in an overshoot of 25.6%, while the overshoot with the VSG is around 67.4%. Moreover, the settling time of the proposed controller is around 2.08 s, whereas that of the VSG is around 4.65 s. Therefore, both the overshoot and settling time with the proposed controller are less than those with the VSG controller. As shown in Fig. 11(a), the change in power output with a droop controller is the most well-tracked out of the three traces shown. Active power output with the droop controller has no overshoot, and the settling time, which is 0.02 s, is significantly lower than the other two controllers.

Fig. 11(b) shows the change in the internal frequency ($\Delta\omega$) following an active power reference change in a strong grid in the GC mode for droop, VSG, and the proposed controllers. Immediately after the active power change, $\Delta\omega$ with the droop controller increases sharply to 50.43 Hz. However, it settles back at 50 Hz quickly around 2.15 s. On the contrary, $\Delta\omega$ with the VSG gradually increases to 0.117 Hz and settles back at 50 Hz within 7.5 s. In contrast, $\Delta\omega$ with the proposed controller gradually increases to 0.071 Hz after the power change and settles back at 50 Hz within 3.2 s. Therefore, the peak and settling time of $\Delta\omega$ following an active power change with the VSG is much higher than that of the proposed controller.

*2) Weak Grid Scenario (SCR = 2):* The experimental results for the active power reference change in the GC mode in a weak grid are shown in Fig. 12. As shown in Fig. 12(a), the experimental results validate the superior performance of the proposed controller over the droop and VSG controllers in a weak grid in the GC mode. The proposed controller results in an overshoot of 32%, whereas the overshoot with the VSG is around 38%. Moreover, the settling time of the proposed controller is around 5.8 s, whereas that of the VSG is around 6.1 s. Hence, both the overshoot and settling time with the proposed controller are less than those with the VSG

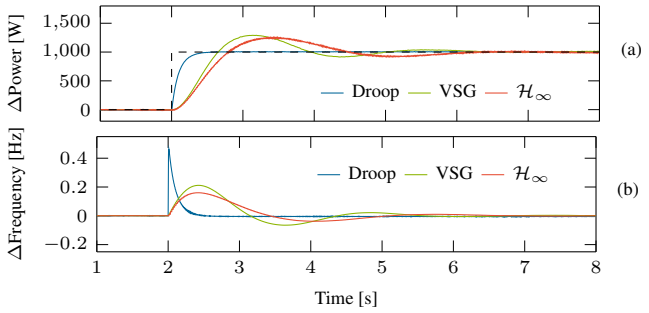


Fig. 12. Experimental results for a 1 kW step change in active power reference in the GC mode for a grid with an SCR = 1.9: (a) step response of active power and (b) change in frequency.

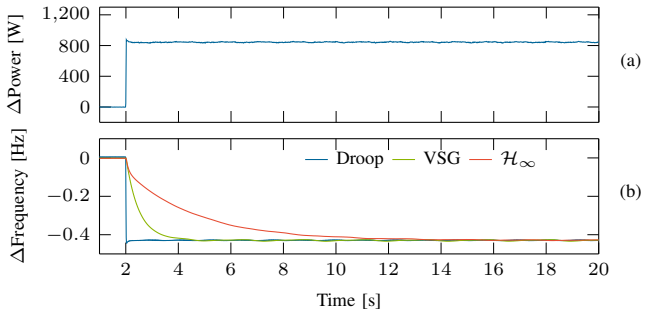


Fig. 13. Experimental results for a load disturbance of 850 W in the SA mode: (a) change in active power and (b) change in frequency.

controller. As shown in Fig. 12(a), similar to the strong grid scenario, the power output change with a droop controller is the most well-tracked out of the three traces shown. Active power output with the droop controller has no overshoot, and the settling time, which is around 2.81 s, is significantly less than the other two controllers.

Fig. 12(b) shows $\Delta\omega$ following an active power reference change in a weak grid in the GC mode for the droop, VSG, and the proposed controller. Immediately after the active power change, $\Delta\omega$ with the droop controller increases sharply to 50.45 Hz. However, it settles back at 50 Hz quickly around 3.05 s. In contrast, $\Delta\omega$ following a change in active power with the VSG and the proposed controller are approximately similar. $\Delta\omega$ with the VSG gradually increases to 0.211 Hz and settles back at 50 Hz within 6 s. Similarly, $\Delta\omega$ with the proposed controller gradually increases to 0.16 Hz after the power change and settles back at 50 Hz within 5.8 s. Therefore, the peak and settling time of $\Delta\omega$ following an active power change with the VSG is slightly higher than that of the proposed controller.

As shown in Fig. 11 and 12, the performance of the proposed controller is better than the VSG controller for a wide range of grid conditions. The overshoot and the settling time are both less in the step response with the proposed controller than that of the VSG controller for a range of grid conditions. Furthermore, as shown in Fig. 11(a) and 12(a), the step response of the proposed controller is much more robust to a wide variety of grid conditions compared to the VSG controller. Another important feature of the proposed controller is that the damping increases as the grid strength increases. As shown in Fig. 11(a) and 12(a), the performance of the step response with the VSG controller deteriorates as the grid strength is increased. When the grid strength is high, the grid impedance is low. Therefore, large power swings could occur even for very small angle deviations [38], [39]. However, as shown in Fig. 11(a), the proposed controller significantly outperforms the VSG controller as the strength of the grid increases.

### *B. Enhanced Virtual Inertia Provision for RoCoF Relay Limit Compliance in the Standalone Mode*

An experiment is conducted on the experimental setup to corroborate the superior performance of the proposed controller over the VSG controller in the SA mode. To this end, the test system shown in Fig. 1 is operated in the SA mode. At t = 2 s, $SW_2$ is closed, and $L_2$ is connected to induce a load disturbance of size 850 W. Fig. 13 shows the experimental results for a load disturbance in the SA mode with the VSG controller and the proposed controller. Fig. 13(a) shows the load disturbance of the size 850 W applied at t = 2 s. The experimental results for frequency variations following a load disturbance in the SA mode with droop, VSG, and proposed controller are presented in Fig. 13(b).

As shown in Fig. 13(b), the frequency variation subsequent to a load disturbance with the droop controller is extremely fast, which is mainly attributed to the high bandwidth of the droop controller. Therefore, the initial RoCoF is extremely high and violates the RoCoF constraint considered in this study. High RoCoF levels are detrimental to some equipment and could trigger the tripping of sources that are highly sensitive to high RoCoF levels. On the other hand, the control parameters of the VSG controller are set such that the initial RoCoF with the VSG controller complies with the RoCoF relay withstand capability limit considered in this paper, which is 1 Hz/s. Therefore, the initial RoCoF with the VSG controller complies with the withstand capability of the RoCoF relays considered in this study. Thus, the frequency trajectory with the VSG controller can be considered as a guide to assess whether the RoCoF with the proposed controller is within the considered RoCoF relay withstand capability. As shown in Fig. 13(b), immediately after load disturbance, the RoCoF with the proposed controller is close to the RoCoF with the VSG controller. However, the RoCoF is considerably low compared to the VSG after some time following the load disturbance. In other words, the proposed controller provides more virtual inertia to the system than the VSG. Therefore, the experimental results verify that the proposed controller adheres to the RoCoF relay withstand capability considered in this paper. Furthermore, as shown in Fig. 13(b), the virtual inertia provision is enhanced with the proposed controller, as the frequency change over time is much slower than that with the VSG controller.

### *C. Frequency Support Capability*

Another important feature of the proposed controller is the ability to support the grid during frequency disturbances. This

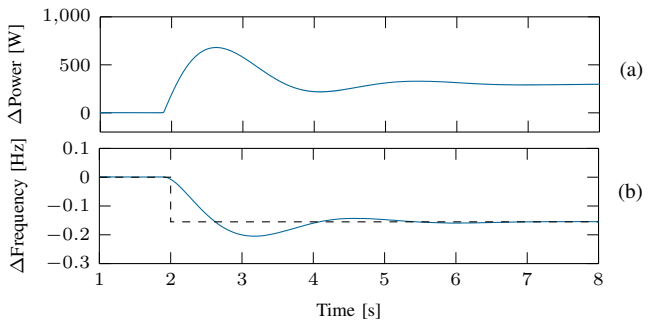


Fig. 14. Experimental results for a grid frequency change of -0.15 Hz with the proposed controller: (a) the change in active power and (b) the change in frequency.

is facilitated in the control design by choosing a desirable gain for the controller using (22). In this paper, a $P-\omega$ droop coefficient of $\pi$/1000 is considered. An experiment is conducted to verify the ability of the proposed controller to support the grid during grid frequency changes. To this end, the test system shown in Fig. 1 is operated in the GC mode. Next, at t = 2 s, the grid frequency is stepped down to 49.85 Hz. The main objective of this test is to check whether the proposed controller injects active power into the grid when the frequency of the grid drops below the nominal frequency. Thereby, the GFMI supports the grid to bring the frequency back to the nominal value.

The experimental results for the frequency support capability of the proposed controller are shown in Fig. 14. Fig. 14(a) shows the active power injection following the grid frequency drop. As the grid frequency is dropped by -0.15 Hz, the GFMI must inject 300 W according to the $P-\omega$ droop coefficient of $\pi$/1000 of the GFMI. As shown in Fig. 14(a), the steady-state power injection of the GFMI settles around 300 W. Therefore, the experimental results verify that the proposed controller is capable of supporting the grid during grid frequency variations according to the desired $P-\omega$ droop coefficient. Furthermore, Fig. 14(b) shows that the internal frequency of the GFMI accurately tracks the grid frequency change of -0.15 Hz and remains synchronized with the grid following the grid frequency change.

### *D. Multi-inverter Test*

The proposed control design is capable of simultaneously designing controllers for multiple inverters in a network. To design multiple controllers, the test network in Fig. 15 is used. The design steps are identical to the control design process described in Section II. However, when multiple inverters are considered $G$, $K$, $W_1$, and $W_2$ are defined as n×n matrix transfer functions instead of individual transfer functions. n is the number of inverters in the network. For the test network shown in Fig. 15, n = 2. As such, $G$ is defined as

$$G = \begin{bmatrix} G_1 & 0 \\ 0 & G_2 \end{bmatrix}, \tag{32}$$

where $G_1$ and $G_2$ are the corresponding system transfer functions of each inverter. The controller transfer function matrix is defined as

$$K = \begin{bmatrix} K_1 & 0 \\ 0 & K_2 \end{bmatrix}, \tag{33}$$

where $K_1$ and $K_2$ are the corresponding controller transfer functions of each inverter. The performance weighting function $W_1$ is defined as

$$W_1 = \begin{bmatrix} W_1^1 & 0 \\ 0 & W_1^2 \end{bmatrix}, \tag{34}$$

where $W_1^1$ and $W_1^2$ are the individual performance weighting functions of each inverter. Finally, the performance weighting function $W_2$ is defined as

$$W_2 = \begin{bmatrix} W_2^1 & 0 \\ 0 & W_2^2 \end{bmatrix}, \tag{35}$$

where $W_2^1$ and $W_2^2$ are the individual performance weighting functions of each inverter. Furthermore, the $P-\omega$ droop gains of each individual inverter ($\mathrm{D_p^1}$ and $\mathrm{D_p^2}$) are evaluated as

$$\begin{bmatrix} \dfrac{x_2^1+x_1^1+x_0^1}{1+y_1^1+y_0^1} & 0 \\ 0 & \dfrac{x_2^2+x_1^2+x_0^2}{1+y_1^2+y_0^2} \end{bmatrix} = \begin{bmatrix} \mathrm{D_p^1} & 0 \\ 0 & \mathrm{D_p^2} \end{bmatrix}, \tag{36}$$

where [$x_2^1$,$x_1^1$,$x_0^1$] and [$x_2^2$,$x_1^2$,$x_0^2$] are the numerator coefficients of the controllers of INV1 and INV2, respectively, and [$y_1^1$,$y_0^1$] and [$y_1^2$,$y_0^2$] are the denominator coefficients of the controllers of INV1 and INV2, respectively.

The ratings of INV1 and INV2 are identical, and they are equal to 1 kW. INV1 and INV2 have a droop coefficient of 1%. Therefore, $\mathrm{D_p}$ of INV1 and INV2 is $\pi$/1000. Both INV1 and INV2 are connected to a load ($\mathrm{L_3}$) through a resistance ($\mathrm{R_g}$) and an inductance ($\mathrm{L_g}$) of 0.15 Ω and 5.18 mH, respectively. The controllers for INV1 and INV2 are designed based on the proposed approach described before. To design the controllers for this system, the data given in Table III are used. As INV1 and INV2 have similar parameters, similar specifications are used during the design. However, note that the control design described above is general. As such, the proposed control design is applicable even if the inverters have different parameters. The frequency responses of $\frac{1}{W_2}$, the 2×2 initial controller $K_c$, and the resulting $K$ are shown in Fig. 16. Note that the high-frequency gain of the $K$ stays below that of $\frac{1}{W_2}$ to adhere to the RoCoF relay withstand limit specified during the control design stage.

Next, the performance of the designed controllers is experimentally validated. Initially, INV1 and INV2 feed the load $\mathrm{L_3}$ of size 450 W. At t = 2 s, the load $\mathrm{L_4}$ of size 850 W is connected to the GFMIs to introduce a load disturbance in the multi-inverter setup. The experimental results are shown in Fig. 17. The change in output power and the corresponding frequency of INV1 and INV2 are shown in Fig. 17(a) and 17(b), respectively. As shown in Fig. 17(a), INV1 and INV2 equally share the load disturbance of 850 W due to their droop coefficients being weighted according to their ratings.

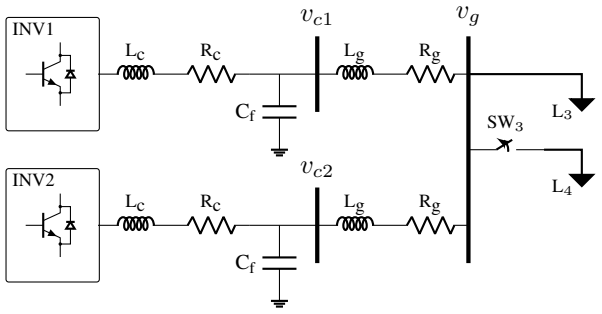


Fig. 15. Test system used for multi-inverter test.

Therefore, both INV1 and INV2 increase their power output by 425 W. Hence, as shown in Fig. 17(a), the proposed controller design facilitates steady-state power sharing. Furthermore, the proposed controllers are designed such that the initial RoCoF following a load disturbance conforms to a RoCoF relay limit of 1 Hz/s up to a disturbance size corresponding to their ratings. As shown in Fig. 17(b), since INV1 and INV2 appropriately share the load disturbance, the RoCoF after the disturbance conforms to the RoCoF relay limit of 1 Hz/s.

### *E. Voltage Disturbance Ride-through Capability*

In this test, the ride-through capability of the controller during a voltage disturbance in GC mode is validated. At t = 0 s, the inverter is injecting an active power of 200 W in the GC mode. Then, the grid voltage ($v_g$) is changed to 0.9 per unit (p.u.) and 1.1 p.u. at t = 2 s and t = 6 s, respectively. Variations in $d$ axis grid voltage ($\mathrm{V_{gd}}$) and capacitor voltage ($\mathrm{V_{cd}}$) are shown in Fig. 18(a). When $\mathrm{V_{gd}}$ is sagged to 0.9 p.u. at t = 2 s, $\mathrm{V_{cd}}$ is also sagged. Similarly, when $\mathrm{V_{gd}}$ is increased to 1.1. p.u. at t = 6 s, $\mathrm{V_{cd}}$ is increased. Corresponding variations in $P$ and $Q$ to the grid voltage disturbance are shown in Fig. 18(b). As shown in Fig. 18(b), the inverter injects approximately 200 VAR of $Q$ in response to the $\mathrm{V_{gd}}$ sag at t = 2 s. This, in turn, assists the grid voltage recovery of the grid. Similarly, as shown in Fig. 18(b), to assist the grid voltage recovery, the inverter absorbs approximately 200 VAR of $Q$ in response to the $\mathrm{V_{gd}}$ increase at t = 6 s. The inverter maintains the $P$ injection to the grid at 200 W during the disturbances. This helps the grid to maintain the uninterrupted supply to the loads during the voltage disturbances. Therefore, this test validates the performance of the proposed controller during voltage disturbances.

## IV. Conclusion

GFMIs are recently becoming highly recognized due to their grid-forming capability in the SA mode and superior performance over GFLIs in weak grids. An $\mathcal{H}_\infty$-based method to design the APC of the GFMIs that meet the performance specifications in both GC and SA modes is proposed in this paper. The proposed control design method can work with both parametric and experimentally identified non-parametric models of the system. Therefore, the proposed control design facilitates a fully data-driven control design approach in which the frequency response of the system is identified using only the input and output data. The presented control design methodology allows classical performance specifications such as maximum closed-loop response time, maximum overshoot, and maximum RoCoF in the SA mode to be easily formulated as constraints in the frequency domain in the design process. The simulation and experimental results validate the superior performance of the proposed controller compared to the VSG and droop controllers. The experimental results show that the step response for a power reference change in the GC mode with the proposed controller is well-damped, and the settling time is short. Furthermore, the proposed controller outperforms the VSG controller for a wide range of grid conditions. The performance of the proposed controller is robust to grid parameter variations in contrast to the performance of the VSG controller over the grid parameter variations. Moreover, the proposed controller conforms to the RoCoF relay withstand limit, and the virtual inertia provision is higher than that of the VSG controller.

## References

[1] C. Yang, L. Huang, H. Xin, and P. Ju, "Placing Grid-Forming Converters to Enhance Small Signal Stability of PLL-Integrated Power Systems," *IEEE Trans. Power Syst.*, vol. 36, no. 4, pp. 3563–3573, 2021.

[2] A. Tayyebi, D. Groß, A. Anta, F. Kupzog, and F. Dörfler, "Frequency Stability of Synchronous Machines and Grid-Forming Power Converters," *IEEE Trans. Emerg. Sel. Topics Power Electron.*, vol. 8, no. 2, pp. 1004–1018, 2020.

[3] D. B. Rathnayake, M. Akrami, C. Phurailatpam, S. P. Me, S. Hadavi, G. Jayasinghe, S. Zabihi, and B. Bahrani, "Grid Forming Inverter Modeling, Control, and Applications," *IEEE Access*, vol. 9, pp. 114 781–114 807, 2021.

[4] M. C. Chandorkar, D. M. Divan, and R. Adapa, "Control of Parallel Connected Inverters in Standalone AC Supply Systems," *IEEE Trans. Ind. Appl.*, vol. 29, no. 1, pp. 136–143, 1993.

[5] H. Nikkhajoei and R. H. Lasseter, "Distributed Generation Interface to the CERTS Microgrid," *IEEE Trans. Power Del.*, vol. 24, no. 3, pp. 1598–1608, 2009.

[6] J. M. Guerrero, J. Matas, L. Garcia de Vicuna, M. Castilla, and J. Miret, "Decentralized Control for Parallel Operation of Distributed Generation Inverters Using Resistive Output Impedance," *IEEE Trans. Ind. Electron.*, vol. 54, no. 2, pp. 994–1004, 2007.

[7] J. M. Guerrero, Luis Garcia de Vicuna, J. Matas, M. Castilla, and J. Miret, "Output Impedance Design of Parallel-connected UPS Inverters with Wireless Load-sharing Control," *IEEE Trans. Ind. Electron.*, vol. 52, no. 4, pp. 1126–1135, 2005.

[8] L. Huang, H. Xin, and F. Dörfler, "$\mathcal{H}_\infty$-Control of Grid-Connected Converters: Design, Objectives and Decentralized Stability Certificates," *IEEE Trans. Smart Grid*, vol. 11, no. 5, pp. 3805–3816, 2020.

[9] H. Beck and R. Hesse, "Virtual Synchronous Machine," in *2007 9th International Conference on Electrical Power Quality and Utilisation*, 2007.

[10] J. Driesen and K. Visscher, "Virtual Synchronous Generators," in *2008 IEEE Power and Energy Society General Meeting - Conversion and Delivery of Electrical Energy in the 21st Century*, 2008.

[11] L. Zhang, L. Harnefors, and H. Nee, "Power-Synchronization Control of Grid-Connected Voltage-Source Converters," *IEEE Trans. Power Syst.*, vol. 25, no. 2, pp. 809–820, 2010.

[12] W. Zhang, A. M. Cantarellas, J. Rocabert, A. Luna, and P. Rodriguez, "Synchronous Power Controller With Flexible Droop Characteristics for Renewable Power Generation Systems," *IEEE Trans. Sustain. Energy*, vol. 7, no. 4, pp. 1572–1582, 2016.

[13] Q. Zhong and G. Weiss, "Synchronverters: Inverters that Mimic Synchronous Generators," *IEEE Trans. Ind. Electron.*, vol. 58, no. 4, pp. 1259–1267, 2011.

[14] A. Karimi, Y. Khayat, M. Naderi, T. Dragičević, R. Mirzaei, F. Blaabjerg, and H. Bevrani, "Inertia Response Improvement in AC Microgrids: A Fuzzy-Based Virtual Synchronous Generator Control," *IEEE Trans. Power Electron.*, vol. 35, no. 4, pp. 4321–4331, 2020.

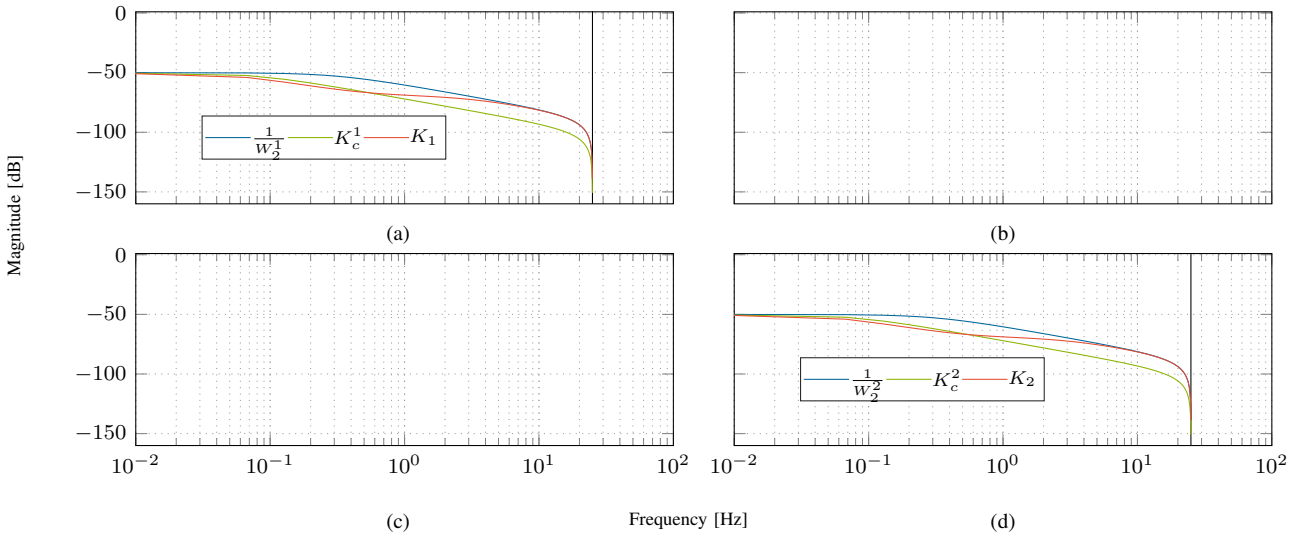


Fig. 16. The frequency responses of $\frac{1}{W_2}$, $K_c$, and $K$

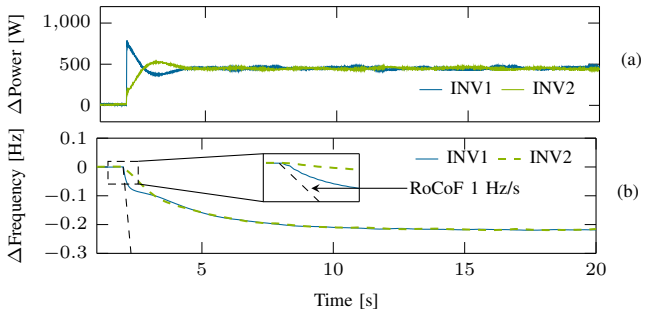


Fig. 17. Experimental results for a load disturbance of 1.5 kW in a multi-inverter network in SA mode: (a) step response of active power and (b) change in frequency.

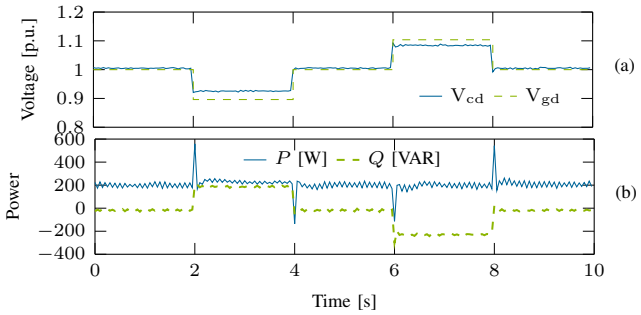


Fig. 18. Experimental results for a voltage disturbance of 0.9 p.u. and 1.1 p.u. in the GC mode: (a) $d$ axis grid and capacitor voltages and (b) change in active power and reactive power.


[15] X. Quan, A. Q. Huang, and H. Yu, "A Novel Order Reduced Synchronous Power Control for Grid-Forming Inverters," *IEEE Trans. Ind. Electron.*, vol. 67, no. 12, pp. 10 989–10 995, 2020.

[16] G. N. Baltas, N. B. Lai, L. Marin, A. Tarrasó, and P. Rodriguez, "Grid-Forming Power Converters Tuned Through Artificial Intelligence to Damp Subsynchronous Interactions in Electrical Grids," *IEEE Access*, vol. 8, pp. 93 369–93 379, 2020.

[17] J. Roldán-Pérez, A. Rodríguez-Cabero, and M. Prodanovic, "Design and Analysis of Virtual Synchronous Machines in Inductive and Resistive Weak Grids," *IEEE Trans. Energy Convers.*, vol. 34, no. 4, pp. 1818–1828, 2019.

[18] M. Ebrahimi, S. A. Khajehoddin, and M. Karimi-Ghartemani, "An Improved Damping Method for Virtual Synchronous Machines," *IEEE Trans. Sustain. Energy*, vol. 10, no. 3, pp. 1491–1500, 2019.

[19] L. Harnefors, M. Hinkkanen, U. Riaz, F. M. M. Rahman, and L. Zhang, "Robust Analytic Design of Power-Synchronization Control," *IEEE Trans. Ind. Electron.*, vol. 66, no. 8, pp. 5810–5819, 2019.

[20] X. Meng, J. Liu, and Z. Liu, "A Generalized Droop Control for Grid-Supporting Inverter Based on Comparison Between Traditional Droop Control and Virtual Synchronous Generator Control," *IEEE Trans. Power Electron.*, vol. 34, no. 6, pp. 5416–5438, 2019.

[21] C. Kammer and A. Karimi, "Decentralized and Distributed Transient Control for Microgrids," *IEEE Trans. Control Syst. Technol.*, vol. 27, no. 1, pp. 311–322, 2019.

[22] D. B. Rathnayake, R. Razzaghi, and B. Bahrani, "Generalized virtual synchronous generator control design for renewable power systems," *IEEE Trans. Sustain. Energy*, 2022.

[23] W. Du, Z. Chen, K. P. Schneider, R. H. Lasseter, S. Pushpak Nandanoori, F. K. Tuffner, and S. Kundu, "A Comparative Study of Two Widely Used Grid-Forming Droop Controls on Microgrid Small-Signal Stability," *IEEE Trans. Emerg. Sel. Topics Power Electron.*, vol. 8, no. 2, pp. 963–975, 2020.

[24] Z. Qu, J. C.-H. Peng, H. Yang, and D. Srinivasan, "Modeling and analysis of inner controls effects on damping and synchronizing torque components in vsg-controlled converter," *IEEE Trans. Energy Convers.*, vol. 36, no. 1, pp. 488–499, 2021.

[25] E. Coelho, P. Cortizo, and P. Garcia, "Small-signal Stability for Parallel-connected Inverters in Stand-alone AC Supply Systems," *IEEE Transactions on Industry Applications*, vol. 38, no. 2, pp. 533–542, 2002.

[26] X. Guo, Z. Lu, B. Wang, X. Sun, L. Wang, and J. M. Guerrero, "Dynamic Phasors-Based Modeling and Stability Analysis of Droop-Controlled Inverters for Microgrid Applications," *IEEE Trans. Smart Grid*, vol. 5, no. 6, pp. 2980–2987, 2014.

[27] AURECON, "Hornsdale Power Reserve: Year 1 Technical and Market Impact Case Study," AURECON, Tech. Rep., Aug. 2018. [Online]. Available: https://www.aurecongroup.com/%20markets/energy/hornsdale-power-reserve-impact-study

[28] L. Xiong, X. Liu, D. Zhang, and Y. Liu, "Rapid power compensation based frequency response strategy for low inertia power systems," *IEEE Trans. Emerg. Sel. Topics Power Electron.*, 2020.

[29] N. Zhou, J. Pierre, and J. Hauer, "Initial Results in Power System Identification from Injected Probing Signals using a Subspace Method," *IEEE Trans. Power Syst.*, vol. 21, no. 3, pp. 1296–1302, 2006.

[30] I. Kamwa, G. Trudel, and L. Gerin-Lajoie, "Low-order Black-box Models for Control System Design in Large Power Systems," in *Proceedings*

*of Power Industry Computer Applications Conference*, 1995, pp. 190–198.

[31] B. Miao, R. Zane, and D. Maksimovic, "System identification of power converters with digital control through cross-correlation methods," *IEEE Trans. Power Electron.*, vol. 20, no. 5, pp. 1093–1099, 2005.

[32] B. Bahrani, "Advanced Control Strategies for Voltage Source Converters in Microgrids and Traction Networks," Ph.D. dissertation, IEL, EPFL, Lausanne, 2012. [Online]. Available: http://infoscience.epfl.ch/record/181221

[33] N. Pogaku, M. Prodanovic, and T. C. Green, "Modeling, Analysis and Testing of Autonomous Operation of an Inverter-Based Microgrid," *IEEE Trans. Power Electron.*, vol. 22, no. 2, pp. 613–625, 2007.

[34] K. Zhou and J. Doyle, *Essentials of Robust Control*. New Jersery: Prentice Hall, 1998.

[35] A. Karimi and C. Kammer, "A Data-driven Approach to Robust Control of Multivariable Systems by Convex Optimization," *Automatica*, vol. 85, pp. 227 – 233, 2017.

[36] J. Löfberg, "YALMIP : a toolbox for modeling and optimization in MATLAB," in *2004 IEEE Int. Conf. on Robotics and Automation (IEEE Cat. No.04CH37508)*, 2004, pp. 284–289.

[37] MOSEK ApS., *The MOSEK Optimization Toolbox for MATLAB Manual v9.2.29*, (2020), Accessed:Aug. 12, 2020. [Online]. Available: https://docs.mosek.com/9.2/toolbox.pdf

[38] X. Wang, M. G. Taul, H. Wu, Y. Liao, F. Blaabjerg, and L. Harnefors, "Grid-synchronization stability of converter-based resources—an overview," *IEEE Open Journal of Industry Applications*, vol. 1, pp. 115–134, 2020.

[39] R. Rosso, X. Wang, M. Liserre, X. Lu, and S. Engelken, "Grid-forming converters: Control approaches, grid-synchronization, and future trends—a review," *IEEE Open Journal of Industry Applications*, vol. 2, pp. 93–109, 2021.


**Dayan B. Rathnayake**